HST Strong-lensing Model for the First JWST Galaxy Cluster SMACS J0723.3−7327

Miriam Golubchik ⓘ, Lukas J. Furtak ⓘ, Ashish K. Meena ⓘ, and Adi Zitrin ⓘ
Physics Department, Ben-Gurion University of the Negev, P.O. Box 653, Be'er-Sheva 84105, Israel; adizitrin@gmail.com

Abstract

On 2022 July 8, NASA shared (https://www.nasa.gov/feature/goddard/2022/nasa-shares-list-of-cosmic-targets-for-webb-telescope-s-first-images) the list of five public showcase targets that have been observed with the new James Webb Space Telescope (JWST) and whose data—at the time of writing—are expected to be released to the public around Tuesday, July 12. One of these targets is the galaxy cluster SMACS J0723.3−7327 ($z = 0.39$), which acts as a gravitational lens and was recently imaged with the Hubble Space Telescope (HST) in the framework of the Reionization Lensing Cluster Survey (RELICS). To facilitate studies by the community with the upcoming JWST data, we publish here a strong-lensing model for SMACS J0723.3−7327—including mass density and magnification maps. We identify five multiple-image families in the HST imaging. For three of them, system membership and redshift are secured by public spectroscopic data. For the remaining two systems, we rely on robust photometric redshift estimates. We use the `Light-Traces-Mass` lens modeling method, which complements the parametric models already available in the RELICS repository and elsewhere and thus helps span a representative range of solutions. The new model published here can be accessed on the RELICS website at MAST. It will be interesting to examine which properties of the mass models change and improve, and by how much, when the JWST data are incorporated.

Unified Astronomy Thesaurus concepts: Strong gravitational lensing (1643); Galaxy clusters (584); High-redshift galaxies (734); Dark matter (353)

1. Introduction

After much anticipation, the first images from the James Webb Space Telescope (JWST) are expected—at the time of writing[1]—to be released to the public starting 2022 July 12. According to the media, these Early Release Observations (ERO; Pontoppidan et al. 2022) will include five targets whose names were published last week by NASA and will be followed by the release of the Director's Discretionary Early Release Science (ERS) programs, e.g., GLASS-JWST (Treu et al. 2022) and CEERS (PI: S. Finkelstein). One of the five ERO targets is SMACS J0723.3−732 (SMACS0723 hereafter), a massive strong-lensing (SL) galaxy cluster that exhibits several gravitationally lensed arcs, as can be seen in recent Hubble Space Telescope (HST) imaging taken in the framework of the Reionization Lensing Cluster Survey (RELICS; Coe et al. 2019). Media reports on upcoming JWST data speculate that these first JWST images will include the deepest imaging of the universe taken to date. While a very deep and impressive Fine Guidance Sensor image may have already qualified for the title, suspicion raises that—thanks to the depth gained by the lensing magnification—these rumors refer to the announced image of SMACS0723. Either way, a detailed SL model is needed to interpret whatever magnified or strongly lensed features will be seen in these new data.

Over the past two to three decades, gravitational lensing has enabled the detection of increasing numbers of faint high-redshift ($z \gtrsim 6$) galaxies (e.g., Franx et al. 1997;

Frye & Broadhurst 1998; Kneib et al. 2004; Bradley et al. 2008; Kashikawa et al. 2011; Zheng et al. 2012; Coe et al. 2013), which currently represent the best candidates for the sources that reionized the universe (Atek et al. 2015). The SL magnification allows us to probe several magnitudes deeper than blank fields, i.e., down to rest-frame UV luminosities $M_{\rm UV} \lesssim -13$ mag (Bouwens et al. 2017; Livermore et al. 2017; Atek et al. 2018; Ishigaki et al. 2018) and stellar masses $M_\star \gtrsim 10^6 M_\odot$ (Bhatawdekar et al. 2019; Kikuchihara et al. 2020; Furtak et al. 2021; Strait et al. 2021). Several high-redshift galaxies have already been detected in SMACS0723 with the HST data from the RELICS program (Salmon et al. 2020; Strait et al. 2021). With the redder wavelength range and greater sensitivity of the JWST, we can expect many more galaxies at even higher redshifts to be detected in the coming months. In order to fully characterize them and study their physical properties, we will need accurate SL magnification models.

At least two lensing models using the `glafic` (Oguri et al. 2010) and `lenstool` (Jullo et al. 2007) codes (see also Fox et al. 2022) have already been generated for SMACS0723 and are publicly available on the RELICS website.[2] In addition, another `lenstool` model was recently constructed (J. Richard, private communication) using similar constraints to those in this work, including the three spectroscopic redshifts from MUSE, and is publicly available online as well.[3] These models are considered *parametric*, in the sense that the cluster galaxies and dark matter (DM) components are assumed to follow known profile shapes, which can be modeled using analytic or parameterized formulae. Here we present a new model with the `Light-Traces-Mass` approach (LTM;

---

[1] 2022 July 10–11; the paper was posted on arXiv before the 18:00 GMT deadline of Monday, 2022 July 11.

[2] https://archive.stsci.edu/prepds/relics/

[3] https://cral-perso.univ-lyon1.fr/labo/perso/johan.richard/ALCS_models/SMACS0723/
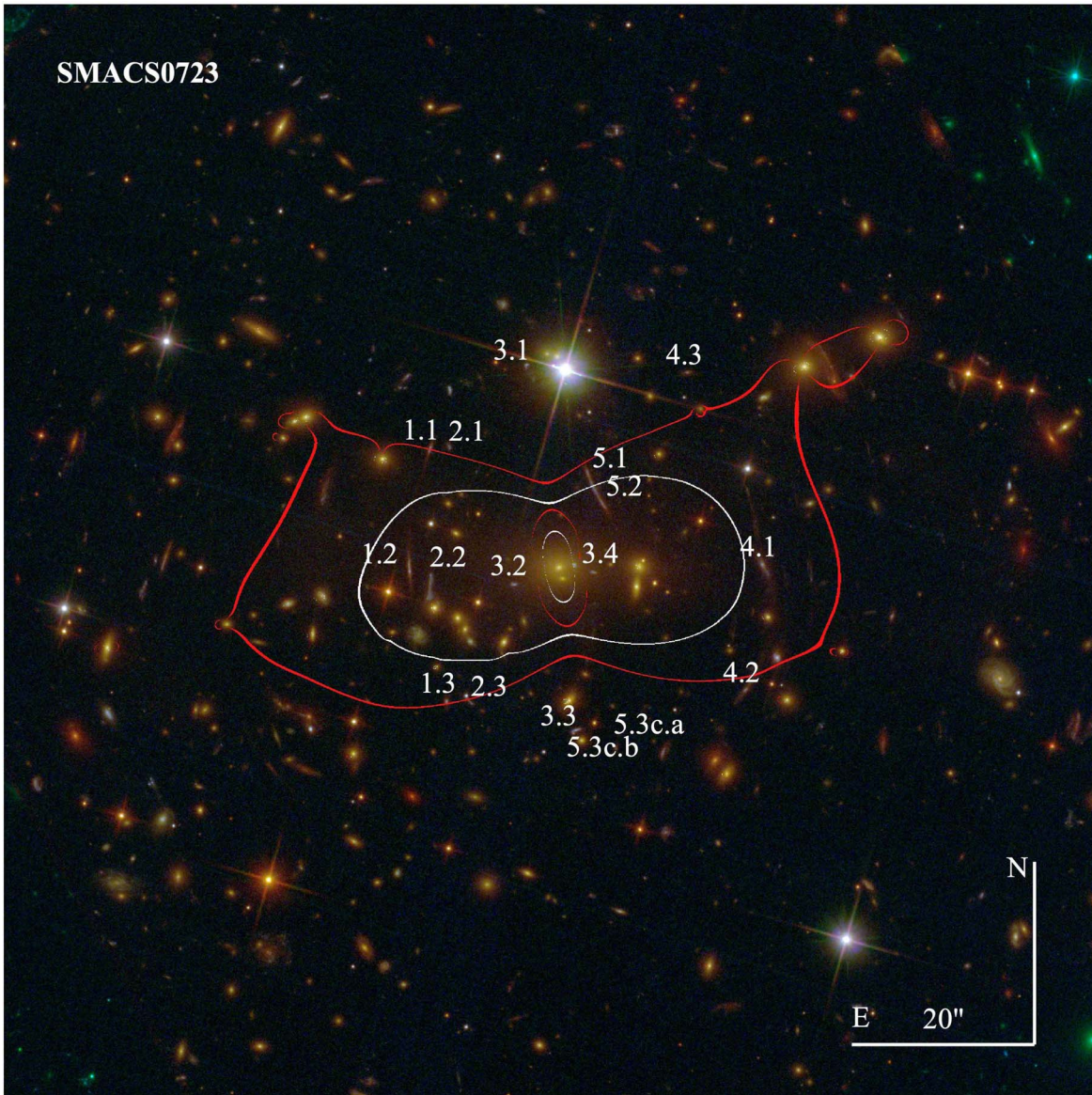
Figure 1. Critical curves and multiple images for SMACS0723 from the `LTM` model (result of this work). Shown is an RGB color-composite image from the RELICS HST data (red = F105W+F125W+F140W+F160W; green = F606W+F814W; blue = F435W). Multiple-image sets are marked on the image, and the critical curves from our model are overlaid in white for a source at the redshift of system 1, $z_{\text{spec}} \simeq 1.45$, and in red for high-redshift objects (nominally for $z = 12$, although the curves are not expected to differ much for other high-redshift sources, say, above $z \gtrsim 7$). Note also that the ellipticity of the mass distribution and critical curves is limited in the `LTM` method, resulting in a high external shear inferred for this cluster, which may not necessarily be real. While we leave a comparison with parametric models for future work, we anticipate that the critical curves would be somewhat more elongated than seen here.

Broadhurst et al. 2005; Zitrin et al. 2009, 2015). On account of being different in nature from parametric techniques, the `LTM` method allows us to probe a different range of solutions. This will be very important for high-redshift studies in this cluster, for which a representative range of possible magnifications for background galaxies are needed. In addition, given the much deeper JWST data and their longer wavelength coverage, we expect that more lensed galaxies will be uncovered soon using these data. This means that the SL models of SMACS0723 can soon be refined further and compared to the pre-JWST version presented in this work.

This paper is organized as follows: In Section 2 we detail the available observations of the cluster and their use in the SL modeling, which is described in Section 3. In Section 4 we present and discuss the results. The work is concluded in Section 5. Throughout this manuscript we use a ΛCDM cosmology with

$\Omega_m = 0.3$, $\Omega_\Lambda = 0.7$, and $H_0 = 70 \, \text{km s}^{-1} \, \text{Mpc}^{-1}$. Unless otherwise stated, we use AB magnitudes (Oke & Gunn 1983) and errors correspond to 1σ.

2. Observations and Data

The galaxy cluster SMACS0723 ($z = 0.39$) is part of the southern extension of the MACS sample (Ebeling et al. 2010; Repp & Ebeling 2018) and was recently observed in the framework of the RELICS program, which observed 41 massive galaxy clusters with HST (PI: D. Coe, Coe 2016) and the Spitzer Space Telescopes (PI: M. Bradac). The RELICS program already achieved its major goals of detecting gravitationally lensed arcs, bright high-redshift galaxies (Salmon et al. 2020; Strait et al. 2021), and various transients (e.g., supernovae presented in Coe et al. 2019; the first spectacular detection of a lensed star at $z \simeq 6.2$
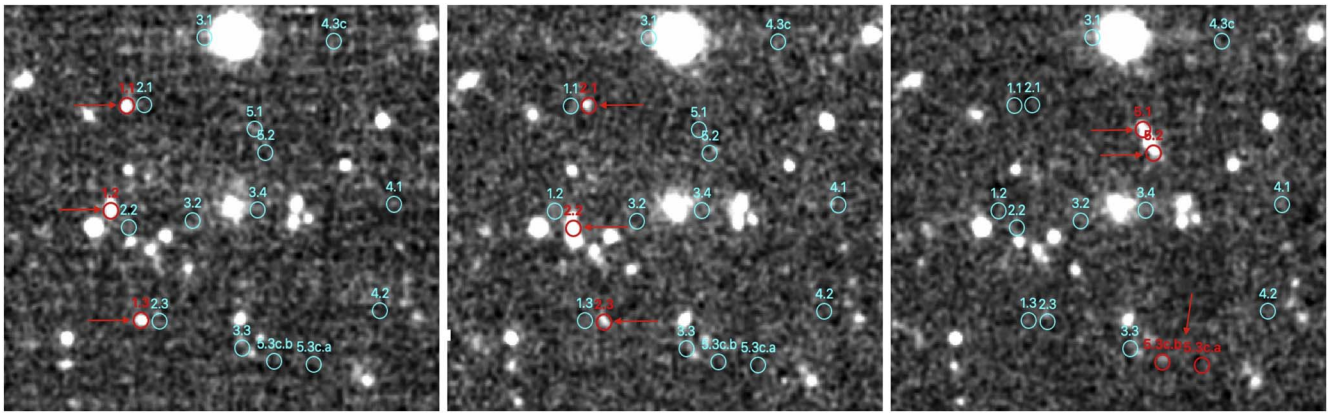
Figure 2. MUSE slices showing the [O II] emission from the three images of system 1 (left; $\lambda \simeq 9134$ Å), the three images of system 2 (middle; $\lambda \simeq 8873$ Å), and the two merging images of system 5 (right; $\lambda \simeq 9040$ Å). Also marked are the two most probable candidates for a third counterimage in system 5 (5.3c).

Table 1
Multiple-image Systems in SMACS0723

ID	R.A. (J2000.0)	Decl. (J2000.0)	z_{phot}	z_{spec}	z_{model}
1.1	7:23:21.7192	−73:27:03.583	1.217 [1.146–1.328]	1.450 ± 0.001	⋯
1.2	7:23:22.2576	−73:27:17.164	1.405 [1.252–1.480]	1.450 ± 0.001	⋯
1.3	7:23:21.3073	−73:27:31.320	1.224 [1.150–1.347]	1.450 ± 0.001	⋯
2.1	7:23:21.2301	−73:27:03.719	1.122 [0.023–1.138]	1.378 ± 0.001	⋯
2.2	7:23:21.7216	−73:27:18.720	⋯	1.378 ± 0.001	⋯
2.3	7:23:20.6700	−73:27:31.666	0.822 [0.026–1.368]	1.378 ± 0.001	⋯
3.1	7:23:19.2740	−73:26:54.830	⋯	⋯	1.27 [1.24–1.30]
3.2	7:23:19.6361	−73:27:18.452	1.147 [1.132–1.415]	⋯	1.27 [1.24–1.30]
3.3	7:23:18.0700	−73:27:34.936	1.227 [1.196–2.330]	⋯	1.27 [1.24–1.30]
3.4	7:23:17.5730	−73:27:17.103	⋯	⋯	1.27 [1.24–1.30]
4.1	7:23:13.2336	−73:27:16.371	2.123 [2.059–2.191]	⋯	2.29 [2.15–2.49]
4.2	7:23:13.6690	−73:27:30.162	2.239 [2.108–2.276]	⋯	2.29 [2.15–2.49]
4.3	7:23:15.1406	−73:26:55.358	2.387 [2.179–2.472]	⋯	2.29 [2.15–2.49]
5.1	7:23:17.6757	−73:27:06.662	0.914 [0.896–0.977]	1.425 ± 0.001	⋯
5.2	7:23:17.3237	−73:27:09.720	0.914 [0.896–0.977]	1.425 ± 0.001	⋯
5.3c_a	7:23:15.7790	−73:27:37.037	1.243 [1.186–1.441]	⋯	⋯
5.3c_b	7:23:16.9814	−73:27:36.522	1.373 [1.214–1.600]	⋯	⋯

Note. Multiple images and candidates. Column (1): ID. Columns (2) and (3): R.A. and decl., in J2000.0. Column (4): photometric redshift. We quote the best photometric redshift from RELICS (see Section 2) and its 95% (2σ) confidence interval. Column (5): for systems 1, 2, and 5 we quote the spectroscopic redshift we measure and use as input; see Section 3.1. Column (6): The redshift of the system as resulting from the SL model. Candidate images whose identification is not secure are marked with "c," namely, the two candidates for image 5.3. Note that these were therefore not used in the minimization.

shown in Welch et al. 2022). Each cluster was observed (in two separate epochs) to about AB mag 26.5 in seven HST bands: F435W, F606W, and F814W with the Advanced Camera for Surveys (ACS), and F105W, F125W, F140W, and F160W with the Wide Field Camera 3 (WFC3). Some clusters also build on previous HST observations (Coe et al. 2019). For SMACS0723, additional HST imaging was taken following supernovae detected in its field, as detailed in Coe et al. (2019). The RELICS data products for SMACS0723 include reduced images and color-composite images, photometric catalogs generated with SExtractor (Bertin & Arnouts 1996), and photometric redshifts computed with the Bayesian Photometric Redshifts code (BPZ; Benítez et al. 2004; Coe et al. 2006). These are publicly available through the RELICS website.[4] We refer the

reader to Coe et al. (2019) for details on the HST data reduction and catalog assembly.

In this work, we also make use of data from the Multi Unit Spectroscopic Explorer (MUSE; Bacon et al. 2010) on ESO's Very Large Telescope (VLT). SMACS0723 was observed with MUSE for 2910 s (Program ID 0102.A-0718; PI: A. Edge), and the data were published on 2019 April 16 on the ESO Science Archive.[5] We use these public data to secure multiple-image families identified in the HST data and measure their spectroscopic redshifts where possible.

Note that SMACS0723 was also observed with the Atacama Large Millimeter/submillimeter Array (ALMA) in Band 6 in the framework of the ALMA Lensing Cluster Survey (ALCS; Kohno 2019). These data, however, are not used in this study.

---

[4] https://relics.stsci.edu/

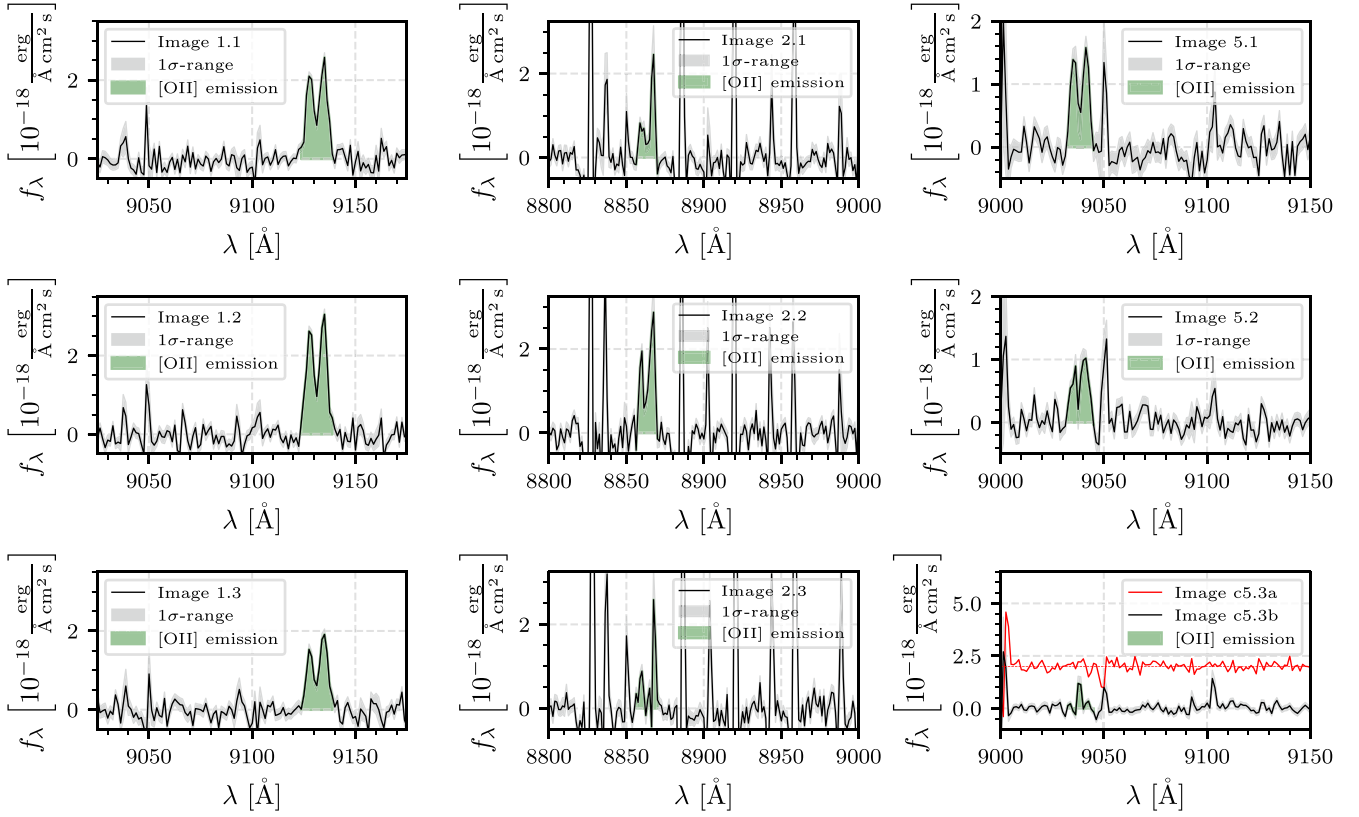[5] http://archive.eso.org/scienceportal/home

Figure 3. Continuum-subtracted MUSE spectra of the multiple-image systems with MUSE detections, collapsed to 1D spectra (black lines). The gray shaded areas represent the 1σ ranges of the measured spectra. Each image system shows a strong double-peaked emission feature (green shaded area) that is consistent with the [O II] $\lambda\lambda3726, 3729$ doublet at redshifts $z \simeq 1.45$, $z \simeq 1.38$, and $z \simeq 1.42$, respectively. Note that there are no significant skylines at the positions of the [O II] doublets. For the two counterimage candidates in system 5, we find a tentative [O II] detection in 5.3c_b but none in 5.3c_a (which we offset vertically by 2×10^{-18} erg cm^{-2} s^{-1} Å^{-1} in the bottom right panel). The possible [O II] detection suggests that 5.3c_b is the true counterimage.

3. SL Modeling of SMACS0723

Our LTM SL model of SMACS0723 takes two components as inputs: the strongly lensed multiple-image systems described in Section 3.1, as SL constraints, and the cluster member galaxies identified in Section 3.2, as a guide for the cluster mass components. We also give a brief summary of our modeling method in Section 3.3.

3.1. Multiple Images

Before running the lens-model minimization, the first tasks we face are the identification of multiple-image families and the measurement of their redshifts. This is done by first searching for multiple images by eye in the HST data and then identifying the counterimages of each system both via their color, internal details, and photometric redshift as measured in the RELICS catalog (see Section 2), and by iteratively using the SL model (see Section 3.3) to determine whether the images of one system map onto the same source. With this procedure, we identify five multiple-image systems in SMACS0723, which are all shown in Figure 1 and listed in Table 1.

Fortunately, we are able to spectroscopically confirm the redshifts of several multiple-image systems, by scanning the MUSE cube of SMACS0723 (see Section 2) for emission lines. As can be seen in Figure 2, systems 1, 2, and 5 each show a strong double-peaked emission line (see also Figure 3) consistently over all images in the system in three different wavelength slices. In all three systems, this emission feature is consistent with the [O II] $\lambda\lambda3726, 3729$ doublet in terms of

both peak separation and redshift. Since the doublets are not completely resolved in the MUSE data (see Figure 3), we fit a simple, single Gaussian to the double peaks in order to measure redshifts based on the center between the two peaks. As a result, we measure spectroscopic redshifts of $z = 1.450 \pm 0.001$, $z = 1.378 \pm 0.001$, and $z = 1.425 \pm 0.001$ for systems 1, 2, and 5, respectively. These are in excellent agreement with the photometric redshifts for these systems and can also be seen in Table 1. In system 5, we find a very weak tentative detection of the [O II] doublet at $z \simeq 1.43$ in the counterimage candidate 5.3c_b but nothing in 5.3c_a (bottom right panel of Figure 3). This indicates that the image candidate c5.3b might be the true counterimage to system 5.[6] Note that we use neither image candidate as a constraint in our SL model.

3.2. Cluster Member Galaxies

In order to identify the cluster galaxies for the mass model, we use the red sequence (Gladders & Yee 2005) of SMACS0723, which stands out in a color–magnitude diagram generated with the F814W and F606W bands (see Figure 4). After a by-eye inspection and removal of interloping objects that are not obvious cluster members, such as stars, we are left with 130 galaxies brighter than 23 mag in the F814W band. These will be included as cluster members in our SL model.

---

[6] Analysis of the new JWST data posterior to the time of writing of this work does indeed confirm 5.3c_b to be the counterimage of system 5 (e.g., Mahler et al. 2022; Pascale et al. 2022).
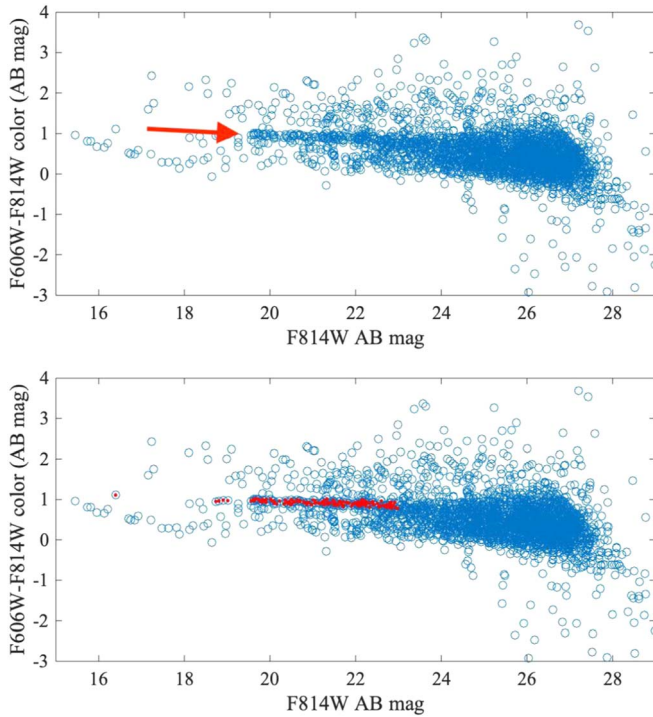
Figure 5. Projected surface mass density of SMACS0723. We show κ, the surface mass density distribution in units of the critical mass density for SL, for the source redshift of system 1, at $z = 1.45$. Note that, in practice, the surface mass density distribution may be more elongated than seen here because the range of possible elongations is limited in the LTM approach and is compensated by an external shear as discussed in the text.

Figure 4. Top panel: color–magnitude diagram of objects detected in the RELICS field of SMACS0723. The cluster's red sequence is clearly visible as a narrow strip, marked here with a red arrow for guidance. Bottom panel: the 130 selected red cluster members used for the modeling are marked with inner red circles. We limit our selection to objects brighter than F814W = 23 AB mag.

3.3. SL Modeling Method

We use the Light-Traces-Mass (LTM) SL modeling method of Zitrin et al. (2009, 2015, and references therein), originally based on Broadhurst et al. (2005). More complete details of the formalism can be found in the above references, and we only give a broad outline here.

A mass model in the LTM formalism consists of three main components. The first component is the total mass density distribution of all central cluster galaxies, each modeled with a simple power-law (q) surface mass density scaled by the galaxy's luminosity. The second component is a DM map that is obtained by smoothing the galaxy mass map with a Gaussian kernel of width S. The two components are then summed together with a relative weight k_{gal}, reflecting the ratio of luminous matter to DM, and the superposition is scaled to a desired redshift by some factor K. The third component contributes to the deflection field but not to the total mass density. It is an external shear of strength γ_{ex} and position angle ϕ_{ex}, which allows for greater effective elongation of the critical curves and can help account for the contribution of larger-scale structure far outside of the range constrained by SL data. The model thus comprises six main parameters: q, S, K, k_{gal}, γ_{ex}, and ϕ_{ex}. Usually, we introduce ellipticities and position angles, as well as central cores, for a few key cluster members, such as the brightest cluster galaxies, which are also the most massive. In addition, it is often useful to leave the relative weight (i.e., the relative mass-to-light ratio) of some key galaxies as free parameters as well. Similarly, the redshift of systems lacking spectroscopic measurement can also be left to be freely optimized. The optimization of the model is carried out by minimizing a χ^2 function that measures the distance between the observed multiple images and their positions predicted by the model. This is done via Markov Chain Monte Carlo (MCMC) with a Metropolis
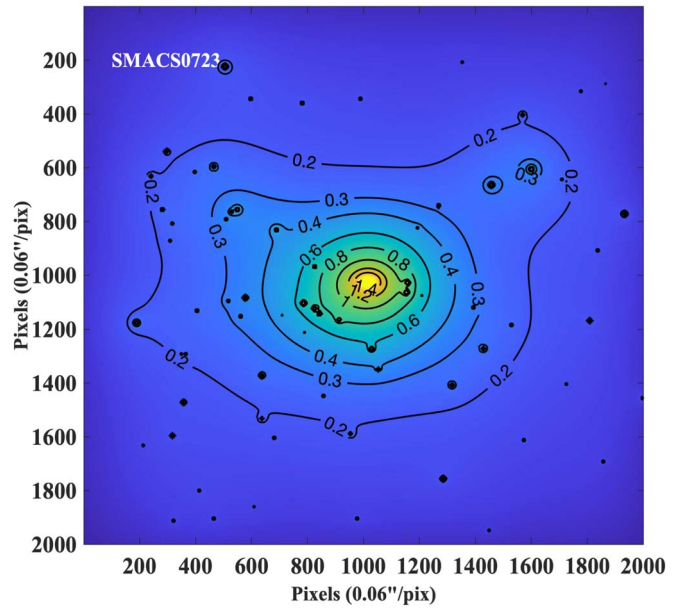
–Hastings algorithm (e.g., Hastings 1970). We also include some annealing in the procedure, and the chain typically runs for several thousand steps after the burn-in stage. Errors are calculated from the same MCMC chain.

For the modeling of SMACS0723, we leave the relative weight of the three brightest galaxies, including the brightest cluster galaxy (BCG), to be freely optimized by the model, although for the second- and third-brightest galaxies we only use a narrow range around the original luminosity. The central core and position angle of the BCG are also left free to be optimized. In addition, the redshifts of systems 3 and 4, whose exact redshifts were not confirmed with the MUSE data (see Section 3.1), are introduced as free parameters as well, using the photometric redshift as a prior. We run a relatively quick model with about 5000 MCMC steps.

4. Results and Discussion

In Figure 1 we show, along with the positions of the multiple images, the critical curves of the resulting best-fit LTM model. We note that the model has a relatively high rms of $1{.}''7$ in reproducing the positions of the multiple images. Although the LTM method often results in somewhat higher rms values than typical parametric methods, since it is coupled to the light distribution, the current rms is relatively high also compared to the number of systems and simplicity of the lensing system. One of the causes may be related to the ellipticity: if the underlying projected mass distribution is significantly elongated, the LTM parameterization itself might not be sufficient to easily reproduce it and usually requires a strong external shear, as is indeed the case here. We obtain an extreme external shear value of $\gamma \simeq 0.3$. While there may be some external shear due to structure outside the field of view, such a high value is usually an indication that the model artificially compensates for the lack of intrinsic ellipticity in its mass distribution: external shear is known to be degenerate with the intrinsic ellipticity of the lens (e.g., Kassiola & Kovner 1993).
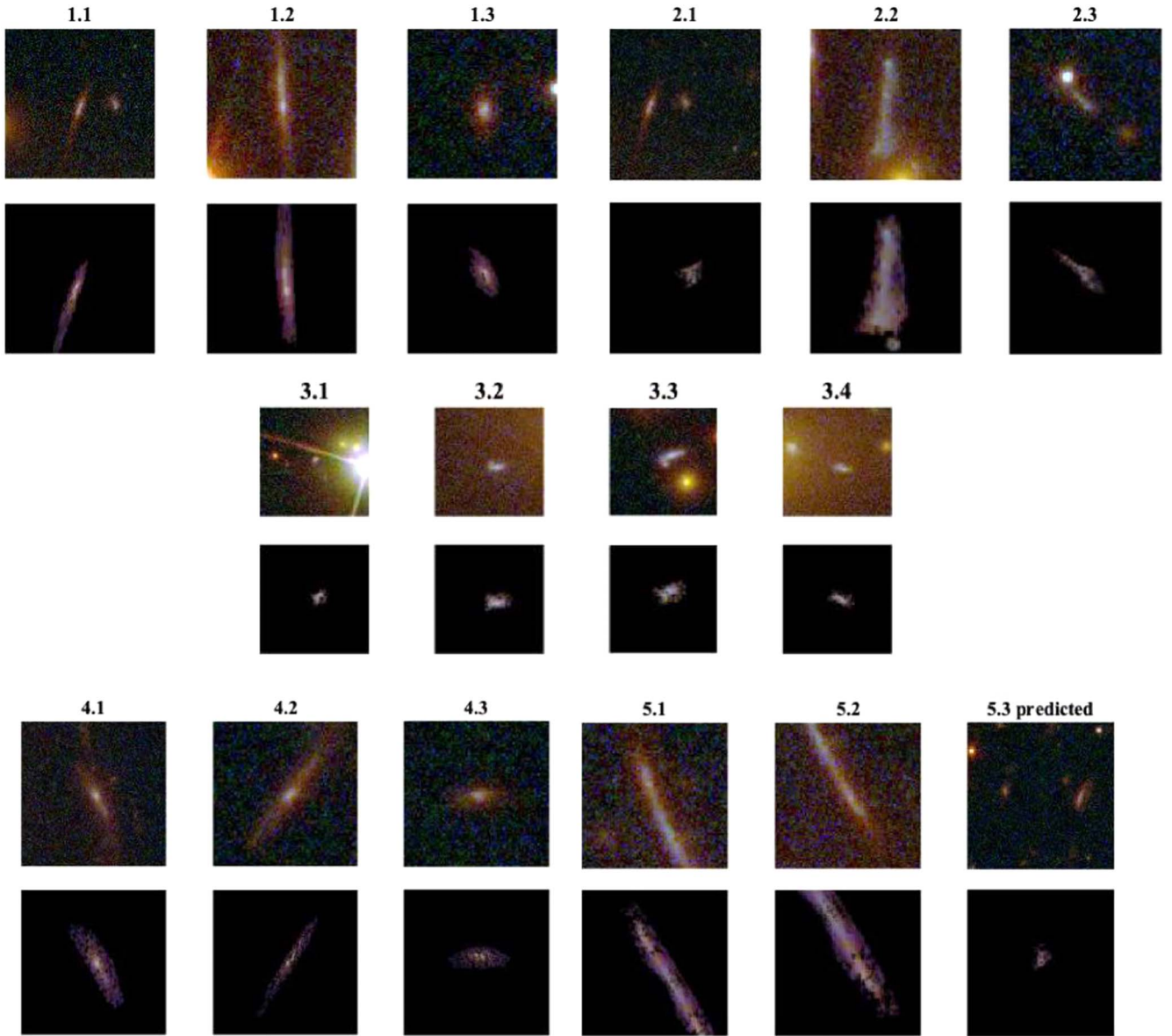
Figure 6. Reproduction of the multiple images in SMACS0723 by our LTM model. For each system, we lens one of the arcs to the source plane and back through the lens to reproduce the other images of the systems. Note that images are slightly smoothed and centered for a better view. Their location in this figure is therefore not an indication of the accuracy of the model. The upper row for each system shows stamp cutouts of the original images, and the bottom row shows the reproduction by the model. In system 5, the third image is predicted, but two options are seen nearby (though see Section 3.1 and Figure 3). Overall, the model seems to reproduce multiple images relatively well.

On galaxy scales, the origin of effective ellipticity of the lens may affect the statistics of double- versus quadruply imaged quasars (e.g., Keeton et al. 1997; Oguri & Marshall 2010; Luhtaru et al. 2021), for example. The degeneracy was also found to exist on galaxy cluster scales (e.g., Zitrin et al. 2015), where a statistical analysis of the 25 CLASH clusters resulted in a relatively similar goodness of fit for parametric models that included ellipticity, versus models that did not, but instead included external shear (although this conclusion may not hold for extreme shear values as in SMACS0723). In practice, the overall ellipticity may generally be a result of both intrinsic ellipticity and external shear. A value of $\gamma \simeq 0.3$, as in our case here, is too extreme to be accounted for solely by a real external component (which also is not visible in the current data), and thus we conclude that it is most likely an indication of high intrinsic ellipticity in the projected mass distribution.

Another reason for the relatively high rms may be related to the mass-to-light ratios of individual galaxies, which strongly impact the LTM solution. Since individual galaxies deviate in practice from the assumed scaling relation, we often leave the weight of bright galaxies free to be optimized. Here we essentially only leave the BCG and two other cluster galaxies to be freely weighted (and within relatively narrow bounds). This likely limits the goodness of fit of the current model. Future iterations should include a broader range of possibilities and can be expected to improve the fit also within the LTM formalism.

While this effect is not expected to be very large, one other limitation on the quoted rms value in the LTM method is the grid resolution. Since the LTM model is coupled to the preset grid resolution (typically HST resolution or a few times lower than that), each included system adds a finite amount to the

rms, which stems from the fact that the relevant lensing quantities are rounded up to the grid's resolution.

The projected surface mass density map, κ, of the best-fit model is shown in Figure 5. As can be seen in the figure, the mass distribution seems fairly relaxed with no significant substructure near the center. This is also in line with the relatively smooth and symmetric critical curve. Note, however, that because the ellipticity of the LTM is limited, the critical curves (and of course the mass distribution) may be more elongated or more elliptical, in reality. Thus, in future works it would be interesting to compare to parametric models in which the ellipticity can be assigned intrinsically to the mass distribution and is thus not as severely limited. In other words, we expect that analytic models would show a more elongated curve than is seen in Figure 1 for our LTM model.

In Figure 6 we show a detailed reproduction of each multiple image we used as constraints (by delensing−relensing one image of each system, to reproduce the other images of that system). As can be clearly seen, and despite the nominal quoted positional rms, the model reproduces very well the various multiple images.

One other feature of SL clusters that is useful for assessing their lensing efficiency is the effective Einstein radius, defined as the radius of a circle whose area corresponds to the area enclosed within the critical curves (i.e., the so-called critical area). The effective Einstein radius that we find for SMACS0723 is rather modest, $14\rlap{.}''5 \pm 2''$ for a source at $z_s = 1.45$. The mass enclosed in this critical area is $(3.42 \pm 0.47) \times 10^{13}\ M_\odot$. For a source redshift of $z_s = 2$, we find $\theta_{\rm E} = 16\rlap{.}''9 \pm 2''$, enclosing $(4.15 \pm 0.58) \times 10^{13}\ M_\odot$. Errors on the effective Einstein radius and enclosed total mass are nominal, systematic values that reflect the typical errors seen between different models. The statistical uncertainties are somewhat smaller. These estimates will be revised when more multiple images are identified in JWST data.

5. Summary

We presented a new HST-based SL model for the massive galaxy cluster SMACS0723 that—according to media—was recently imaged with JWST and whose new data will be published in the next few days (as of the time of writing).

We find a relatively modest lens of $\theta_{\rm E} \simeq 14\rlap{.}''5 \pm 2''$ for a source at $z = 1.45$ and $\theta_{\rm E} \simeq 16\rlap{.}''9 \pm 2''$ for a source at $z = 2$. The mass distribution seems to be relatively relaxed with no major DM substructure close to the cluster center.

The importance of our SL model is twofold: First, it is constructed with a distinct method that is different from typical parametric modeling techniques and thus probes a different region of the solution space than previous models. This will become useful for upcoming studies of the high-redshift galaxy population behind SMACS0723 with the new JWST data. Second, it is made public right before the release of the JWST data of this cluster. Because of the greater depth of the JWST observations, the released imaging data might reveal new multiple-image systems (and high-redshift galaxies), which in turn will increase the number of SL constraints on the DM distribution of the cluster. Given that our current model is "JWST-blind," it will allow for a comparison with future versions that will make use of the new JWST data.

ORCID iDs

Miriam Golubchik ⬮ https://orcid.org/0000-0001-9411-3484
Lukas J. Furtak ⬮ https://orcid.org/0000-0001-6278-032X
Ashish K. Meena ⬮ https://orcid.org/0000-0002-7876-4321
Adi Zitrin ⬮ https://orcid.org/0000-0002-0350-4488

References

Astropy Collaboration, Robitaille, T. P., Tollerud, E. J., et al. 2013, A&A, 558, A33
Atek, H., Richard, J., Jauzac, M., et al. 2015, ApJ, 814, 69
Atek, H., Richard, J., Kneib, J.-P., & Schaerer, D. 2018, MNRAS, 479, 5184
Bacon, R., Accardo, M., Adjali, L., et al. 2010, Proc. SPIE, 7735, 773508
Benítez, N., Ford, H., Bouwens, R., et al. 2004, ApJS, 150, 1
Bertin, E., & Arnouts, S. 1996, A&AS, 117, 393
Bhatawdekar, R., Conselice, C. J., Margalef-Bentabol, B., & Duncan, K. 2019, MNRAS, 486, 3805
Bouwens, R. J., Oesch, P. A., Illingworth, G. D., Ellis, R. S., & Stefanon, M. 2017, ApJ, 843, 129
Bradley, L. D., Bouwens, R. J., Ford, H. C., et al. 2008, ApJ, 678, 647
Broadhurst, T., Benítez, N., Coe, D., et al. 2005, ApJ, 621, 53
Coe, D. 2016, Reionization Lensing Cluster Survey ("RELICS"), MAST, doi:10.17909/T9SP45
Coe, D., Benítez, N., Sánchez, S. F., et al. 2006, AJ, 132, 926
Coe, D., Salmon, B., Bradač, M., et al. 2019, ApJ, 884, 85
Coe, D., Zitrin, A., Carrasco, M., et al. 2013, ApJ, 762, 32
Earl, N., Tollerud, E., Jones, C., et al. 2021, astropy/specutils: V1.5.0, v1.50, Zenodo, doi:10.5281/zenodo.5721652
Ebeling, H., Edge, A. C., Mantz, A., et al. 2010, MNRAS, 407, 83
Fox, C., Mahler, G., Sharon, K., & Remolina González, J. D. 2022, ApJ, 928, 87
Franx, M., Illingworth, G. D., Kelson, D. D., van Dokkum, P. G., & Tran, K.-V. 1997, ApJL, 486, L75
Frye, B., & Broadhurst, T. 1998, ApJL, 499, L115
Furtak, L. J., Atek, H., Lehnert, M. D., Chevallard, J., & Charlot, S. 2021, MNRAS, 501, 1568

Ginsburg, A., Robitaille, T., Beaumont, C., & ZuHone, J. 2014, Release Candidate 2 - includes yt interop, v0.2-rc2, Zenodo, doi:10.5281/zenodo.11485

Gladders, M. D., & Yee, H. K. C. 2005, ApJS, 157, 1

Hastings, W. K. 1970, Biometrika, 57, 97

Hunter, J. D. 2007, CSE, 9, 90

Ishigaki, M., Kawamata, R., Ouchi, M., et al. 2018, ApJ, 854, 73

Jullo, E., Kneib, J.-P., Limousin, M., et al. 2007, NJPh, 9, 447

Kashikawa, N., Shimasaku, K., Matsuda, Y., et al. 2011, ApJ, 734, 119

Kassiola, A., & Kovner, I. 1993, ApJ, 417, 450

Keeton, C. R., Kochanek, C. S., & Seljak, U. 1997, ApJ, 482, 604

Kikuchihara, S., Ouchi, M., Ono, Y., et al. 2020, ApJ, 893, 60

Kneib, J.-P., Ellis, R. S., Santos, M. R., & Richard, J. 2004, ApJ, 607, 697

Kohno, K. 2019, ALMA2019: Science Results and Cross-Facility Synergies (Garching: ESO), 64

Livermore, R. C., Finkelstein, S. L., & Lotz, J. M. 2017, ApJ, 835, 113

Luhtaru, R., Schechter, P. L., & de Soto, K. M. 2021, ApJ, 915, 4

Mahler, G., Jauzac, M., Richard, J., et al. 2022, arXiv:2207.07101

Ofek, E. O. 2014, MAAT: MATLAB Astronomy and Astrophysics Toolbox, Astrophysics Source Code Library, ascl:1407.005

Oguri, M., & Marshall, P. J. 2010, MNRAS, 405, 2579

Oguri, M., Takada, M., Okabe, N., & Smith, G. P. 2010, MNRAS, 405, 2215

Oke, J. B., & Gunn, J. E. 1983, ApJ, 266, 713

Pascale, M., Frye, B. L., Diego, J., et al. 2022, arXiv:2207.07102

Pontoppidan, K., Blome, C., Braun, H., et al. 2022, ApJL, 936, L14

Price-Whelan, A. M., Sipőcz, B. M., Günther, H. M., et al. 2018, AJ, 156, 123

Repp, A., & Ebeling, H. 2018, MNRAS, 479, 844

Salmon, B., Coe, D., Bradley, L., et al. 2020, ApJ, 889, 189

Steinhardt, C. L., Jauzac, M., Acebron, A., et al. 2020, ApJS, 247, 64

Strait, V., Bradač, M., Coe, D., et al. 2021, ApJ, 910, 135

Treu, T., Roberts-Borsani, G., Bradac, M., et al. 2022, ApJ, 935, 110

van der Walt, S., Colbert, S. C., & Varoquaux, G. 2011, CSE, 13, 22

Virtanen, P., Gommers, R., Oliphant, T. E., et al. 2020, NatMe, 17, 261

Welch, B., Coe, D., Diego, J. M., et al. 2022, Natur, 603, 815

Windhorst, R. A., Cohen, S. H., Jansen, R. A., et al. 2022, AJ, submitted, (arXiv:2209.04199)

Zheng, W., Postman, M., Zitrin, A., et al. 2012, Natur, 489, 406

Zitrin, A., Broadhurst, T., Umetsu, K., et al. 2009, MNRAS, 396, 1985

Zitrin, A., Fabris, A., Merten, J., et al. 2015, ApJ, 801, 44